18th National & 7th ISHMT-ASME
Heat and Mass Transfer Conference
January 4-6, 2006
Paper No: **IIT Guwahati, India**

Heat Transfer by Impingement of Circular Free-Surface Liquid Jets

John H. Lienhard V
Department of Mechanical Engineering
Massachusetts Institute of Technology
Cambridge MA 02139-4307 USA
email: lienhard@mit.edu

Abstract

This paper reviews several aspects of liquid jet impingement cooling, focusing on research done in our lab at MIT. Free surface, circular liquid jet are considered. Theoretical and experimental results for the laminar stagnation zone are summarized. Turbulence effects are discussed, including correlations for the stagnation zone Nusselt number. Analytical results for downstream heat transfer in laminar jet impingement are discussed. Splattering of turbulent jets is also considered, including experimental results for the splattered mass fraction, measurements of the surface roughness of turbulent jets, and universal equilibrium spectra for the roughness of turbulent jets. The use of jets for high heat flux cooling is described briefly.

Nomenclature

A_{2n} constants in Eq. (5).
B dimensionless velocity gradient, $2\frac{d}{u_f}\frac{du_e}{dr}$
C_c contraction coefficient for liquid jets, jet cross-sectional area divided by nozzle area.
C_f skin friction coefficient.
d jet diameter, fully contracted (m).
$G(\mathrm{Pr})$ boundary layer function of Prandtl number, Eq. (12).
h local heat transfer coefficient, $q_w/(T_w - T_f)$, (W/m^2 K).
$h(r)$ thickness of axisymmetric liquid sheet (m).
k thermal conductivity of liquid (W/m·K), or rms surface roughness (m).
k^* dimensionless surface roughness, k/d.
l distance between nozzle and target plate (m).
Nu_d local Nusselt number based on jet diameter, $q_w d/k(T_w - T_f)$.
p local pressure in liquid (Pa).
p_∞ ambient pressure (Pa).
p_{stgn} stagnation pressure (Pa).
$p_e(r)$ pressure distribution along the wall (Pa).
P_{2n} Legendre function of $2n$ order.
Pr Prandtl number of liquid.
Q volume flow rate of jet (m^3/s).
Q_s volume flow rate of splattered liquid (m^3/s).
q_w wall heat flux (W/m^2).
r radius coordinate in spherical coordinates, or radius coordinate in cylindrical coordinates (m).
r_h radius at which turbulence is fully developed (m).
r_o radius at which viscous boundary layer reaches free surface (m).
r_t radius at which turbulent transition begins (m).
r_1 radius at which thermal boundary layer reaches free surface (m).
Re_d Reynolds number of circular jet, $u_f d/\nu$.
T liquid temperature (K).
T_f temperature of incoming liquid jet (K).
T_w temperature of wall (K).
T_{sf} liquid surface temperature (K).
u, v liquid velocity components in radial, axial direction of cylindrical coordinates (m/s)
u' rms turbulent velocity fluctuation in jet (m/s).
u_f bulk velocity of incoming jet (m/s).
u_h velocity of liquid sheet averaged across thickness h (m/s).
u_m free surface velocity of liquid sheet (m/s).
$u_e(r)$ radial velocity just above boundary layer (m/s).
V_{max} centerline velocity of incoming jet (m/s).
We_d jet Weber number, $\rho u_f^2 d/\sigma$.

Greek Letters

α thermal diffusivity of liquid (m^2/s).
δ, δ_t momentum, thermal boundary layer thickness (m).
δ_{rms} local rms surface roughness of turbulent jet (m).
η dimensionless wavenumber.
θ polar angle of spherical coordinates.
ν kinematic viscosity of liquid (m^2/s).
ξ fraction of impinging liquid splattered, Q_s/Q.
ρ density of liquid (kg/m^3).
σ liquid-gas surface tension (N/m).
ϕ velocity potential (m^2/s).

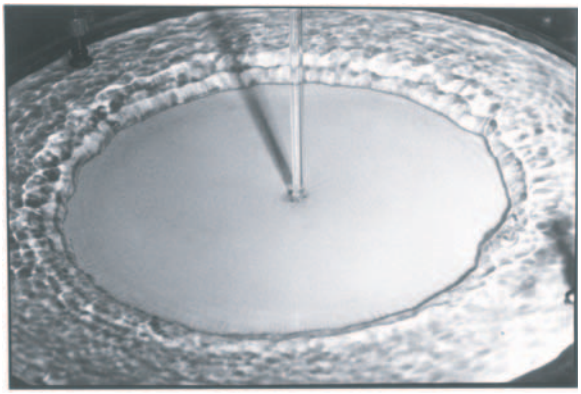

Figure 1: Laminar impinging jet: $\mathrm{Re}_d = 51,000$, $d = 5.0$ mm, sharp-edged orifice, adiabatic target.

1. Introduction

Liquid jet impingement cooling offers very low thermal resistances and is relatively simple to implement. Liquid jets are easily created using a straight tube or a contracting nozzle, and this nozzle can be aimed directly toward the region of a heat load. When the jet strikes the target surface, it forms a very thin stagnation-zone boundary layer which offers little resistance to heat flow. Convective heat transfer coefficients can reach tens of $\mathrm{kW/m^2K}$.

These high heat transfer coefficients make liquid jet impingement attractive in situations where a high heat load must be removed while maintaining a minimum temperature or temperature difference within the system. For example, in some semiconductor laser systems, junction temperatures must be held below 150°C while heat loads may reach $10\ \mathrm{MW/m^2}$. Much attention has been given to jet impingement cooling of electronics.

An impinging jet defines its own flow field, often without the need for added channeling or target modifications. Jets are particularly useful when cooling systems must not add interfering hardware or make structural changes to the cooled object. For example, a fixed nozzle at the end of a processing line can cool each successive item passed under it; and in some automotive engines, oil jets cool the undersides of the piston crowns.

Liquid jets can also carry extremely high heat fluxes, if the velocities are such as to produce a high stagnation pressure. Small diameter water jets at speeds near 130 m/s have removed heat loads of up to $400\ \mathrm{MW/m^2}$. Liquid jets are well-suited for cooling very localized, high-flux heat sources.

The jets of interest in the present article are unsubmerged jets, those that travel through a gas between the nozzle and the target (Fig. 1). These jets are only similar to submerged jets in the stagnation region, and then only when the submerged jet is less than about five diameters in length.

2. Stagnation Zone Theory

Near the point of impact, an impinging jet's fluid flow and heat transfer characteristics are described in general terms by the usual results for the stagnation zone. The flow field can be divided into an outer region of essentially inviscid flow and an inner viscous boundary layer region.

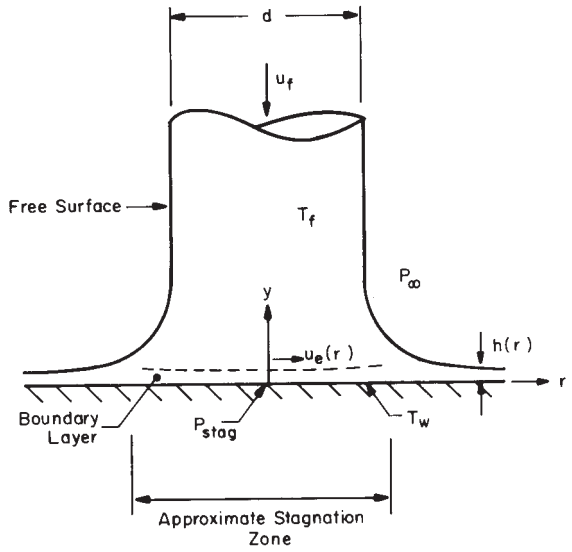

Figure 2: Impinging jet configuration.

The analytical solution of the stagnation zone boundary layer is a classical problem [1, 2, 3], whose results depend primarily on the radial velocity gradient of the inviscid flow near the stagnation point. To adapt stagnation zone boundary layer results to impinging jets, this gradient must be determined. Thus, analysis of the stagnation zone requires first a solution for the inviscid flow of the jet, and then application of the classical boundary solutions for the flow and temperature fields. Together, these lead to expressions for the wall heat flux and the Nusselt number.

2.1 Inviscid Outer Flow

The inviscid flow field of an impinging jet is determined by: a free streamline boundary condition at the liquid surface; an impermeable wall onto which the jet impacts; and assumed forms of the inlet and outlet velocity profiles (Fig. 2). If the inlet profile is irrotational (e.g., uniform), the velocity field can be obtained using potential flow theory ($\nabla^2\phi = 0$); otherwise, the Euler equations must be solved.

In all cases, the stagnation-zone flow has radial velocity distribution at the wall given by

$$u_e(r) = Cr + \cdots, \qquad r \to 0 \tag{1}$$

for $C = (du_e/dr|_{r=0})$ a constant radial velocity gradient. This result is necessitated by the kinematics of any stagnation zone (for irrotational flow, see [4]); the constant C, however, depends on the specific inviscid flow considered. For later use in heat transfer analyses, it is convenient to nondimensionalize the wall gradient:

$$B \equiv 2\frac{d}{u_f}\left.\frac{du_e}{dr}\right|_{r=0} \tag{2}$$

The inviscid flow near the stagnation point has a wall pressure distribution given by

$$p_e(r) = p_\infty + \frac{\rho}{2}\left(u_f^2 - u_e(r)^2\right) \quad (3)$$

$$= p_{stgn} - \frac{\rho}{2}u_e(r)^2 \quad (4)$$

for p_∞ the ambient pressure and p_{stgn} the stagnation pressure. If the jet is nonuniform, u_f refers to the centerline velocity of the jet away from the target; if surface tension pressure is significant, only Eq. 4 applies [5]. Measurements of the wall pressure distribution have often been used to determine $u_e(r)$.

The potential flow is independent of Reynolds number and scales with the inlet speed and jet diameter. Low levels of turbulence in the incoming jet are likely to have only slight effects on the mean velocity distribution outside the wall boundary layer, so the inviscid solutions should apply to either laminar or turbulent jets, if those jets have the specified inlet velocity profiles. In addition, the boundary conditions on the free streamline (no shear stress, pressure constant at p_∞) will apply for steady jets of any density; thus, solutions that have been obtained in the context of nonmixing gas jets (no entrainment of surrounding fluid) apply equally well to unsubmerged liquid jets. The similarity between submerged jets and free liquid jets obviously fails once shear layer instabilities at the freestreamline cause the submerged jet to begin mixing with the surrounding fluid.

2.2 Uniform velocity-profile circular jets

Jets of uniform profile are typical of those created by a sharp-edged orifice several diameters downstream of the outlet and at any Reynolds number well above unity. Analysis and experiments on impingement of such jets date from the late 1920's [6]. Schach [7, 8] obtained approximate solutions for the velocity and experimental measurements of wall pressure; the solutions and pressure data agreed reasonably well in the sense of Eq.(3). Subsequent analytical solutions for normal impingement were found by Shen [9] and by Strand [10].

More recently, the problem has been revisited in detail by Liu, Gabour, and Lienhard [5], who expanded the velocity potential, ϕ, in a series of Legendre polynomials and obtained numerical solutions for the coefficients, incorporating the liquid surface tension. Their result was

$$\frac{\phi(r,\theta)}{(2u_f d)} = \sum_{n=0}^{\infty} A_{2n}\left(\frac{r}{2d}\right)^{2n} P_{2n}(\cos\theta) \quad (5)$$

for spherical coordinates (r,θ) with origin at the stagnation point and polar axis along the axis of the jet. Values of the coefficients are given in Table 1. The velocity along the wall just outside the boundary layer, $u_e(r) = \partial\phi/\partial r|_{\theta=\pi/2}$, is then

$$\frac{u_e(r)}{u_f} = \sum_{n=1}^{\infty} 2nA_{2n}\left(\frac{r}{2d}\right)^{2n-1} P_{2n}(0)$$
$$= (-A_2)\left(\frac{r}{2d}\right) + \left(\frac{3A_4}{2}\right)\left(\frac{r}{2d}\right)^3 + \cdots \quad (6)$$

Table 1: Coefficients of velocity potential [5].

We_d	∞	50	25	16.7
A_2	−1.831	−1.881	−1.944	−2.015
A_4	2.365	2.858	3.469	4.213
A_6	0.5906	−0.01553	−0.8006	−1.825
A_8	−14.81	−19.03	−24.30	−30.78
A_{10}	13.35	20.42	29.38	40.61
A_{12}	50.74	68.74	91.31	119.3

Table 2: Velocity gradients at the stagnation point during laminar circular jet impingement.

Investigators	$B/2$	profile	l/d	We_d
Schach [8]	≈ 0.88	uniform	1.5	∞
Shen [9]	0.743	uniform	1.5	∞
Strand [10]	0.903	uniform	1.0	∞
Liu, Gabour,	0.916	uniform	1.0	∞
Lienhard [5]	0.981	uniform	1.0	50
	1.06	uniform	1.0	25
	1.16	uniform	1.0	16.7
Scholtz and	4.69	parabolic	0.05	∞
Trass [11]			to 0.5	

From this, the dimensionless stagnation-point velocity gradient is

$$B = -A_2 = 1.831 \quad (7)$$

for infinite Weber number; lower Weber number values are shown in Fig. 3. Values of B from the various investigations are compared Table 2.

The velocity and pressure distributions along the wall are shown in Fig. 4. The velocity distribution near the stagnation point can be approximated by a linear distribution

$$\frac{u}{u_f} = \frac{B}{2}\frac{r}{d} = 0.916\,\frac{r}{d}, \quad (8)$$

and the pressure distribution can be estimated using this result and Eq. (3) to within about 10% for $r/d < 0.5$. Heat transfer data suggest that the stagnation zone can reasonably be approximated to extend as far as $r/d \approx 0.7$ from the actual stagnation point. For $r/d > 0.7$, boundary layer growth must be taken into account.

2.3 Parabolic velocity-profile circular jets

Jets of parabolic profile are created by a laminar flow issuing from a long circular tube at Reynolds numbers below 2000–4000. The parabolic profile will diffuse toward a uniform velocity profile as the jet travels to the target, if the jet is long enough for viscosity to act; if the nozzle is within a few diameters of the target, the parabolic distribution should persist.

Inviscid analytical solutions for this case were obtained by Scholtz and Trass [11] for nozzle-to-target

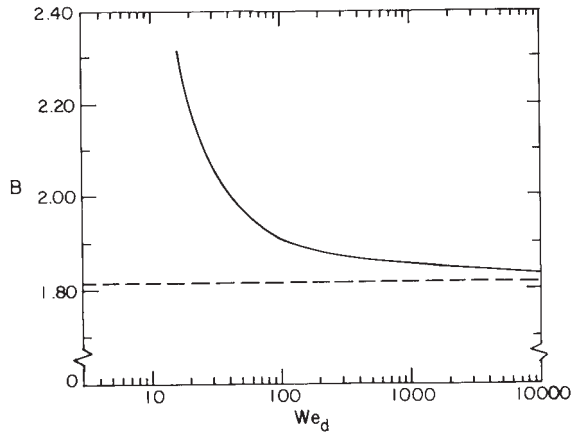

Figure 3: Inviscid stagnation-point velocity gradient, $B = 2(d/u_f)(du_e/dr)$, including effect of Weber number for uniform velocity profile [5].

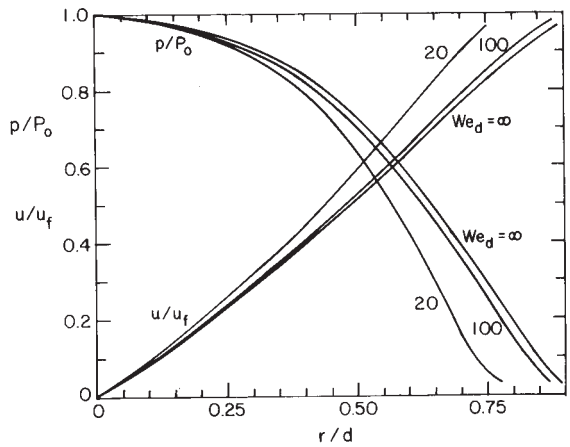

Figure 4: Velocity and pressure variation along the target plate ($y/d = 0$) for an inviscid uniform profile jet at several values of Weber number [5].

spacings of $0.05 < l/d < 0.5$. To leading order, the velocity along the wall near the stagnation point for $l/d = 0.5$ is

$$u_e = 2.323 \left(\frac{V_{max}}{d}\right) r, \quad r/d < 0.4 \tag{9}$$

for V_{max} the maximum (centerline) velocity in the nozzle and d the nozzle diameter. To the accuracy of the numerical solutions, the constant in Eq.(9) is unaffected by l/d in the range $0.05 < l/d < 0.5$. Scholtz and Trass also obtained experimental results for velocity and pressure distributions over the range $0.05 < l/d < 6.0$. The experimental results show little sensitivity to l/d for $l/d > 1$. As the nozzle is moved closer than one diameter from the target, constriction alters the flow field downstream of the stagnation point; however, at the stagnation point itself, the velocity gradient remains unaffected. The experiments showed that the stagnation-point pressure distribution was within 10% of that given by Eqs.(3) and (9) for $r/d < 0.4$ and all nozzle spacings. Note that this is a slightly smaller stagnation zone than is obtained with a uniform jet.

In terms of bulk velocity, $u_f = V_{max}/2$, the dimensionless velocity gradient of the parabolic jet is

$$B = 2\frac{d}{u_f}\left.\frac{du_e}{dr}\right|_{r=0} = 4.646 \tag{10}$$

The experimental results generally support this equation for $0.05 < l/d < 6$. Most importantly, the parabolic-profile jet has a velocity gradient 2.5 times higher than the uniform jet, which raises the heat transfer coefficent substantially.

2.4 Laminar Stagnation-Zone Boundary Layer

Boundary layer theory for the stagnation region is summarized in detail in [12]. As we have seen, u_e is linear in r, and the theory shows that the resulting heat transfer coefficient, h, is independent of r. In other words, the thermal boundary layer has a uniform thickness within the stagnation zone. The uniform value of h also implies that uniform wall temperature and uniform heat flux boundary conditions produce an identical heat transfer coefficient.

From the theory, the Nusselt number depends on the stagnation point velocity gradient as follows:

$$\mathrm{Nu}_d \equiv \frac{hd}{k} = G(\mathrm{Pr})\,\mathrm{Re}_d^{1/2}\sqrt{B} \tag{11}$$

for $\mathrm{Re}_d = u_f d/\nu$. The coefficient $G(\mathrm{Pr})$ (discussed in more detail in [12]) is a function of Prandtl number which can be evaluated numerically. Curve fits can be constructed within given ranges of Pr [13]. For the axisymmetric boundary layer:

$$G(\mathrm{Pr}) \approx \begin{cases} \frac{\sqrt{2\mathrm{Pr}/\pi}}{1+0.804552\sqrt{2\mathrm{Pr}/\pi}} & \text{for } \mathrm{Pr} \le 0.15 \\ 0.53898\,\mathrm{Pr}^{0.4} & \text{for } 0.15 < \mathrm{Pr} < 3.0 \\ 0.60105\,\mathrm{Pr}^{1/3} - 0.050848 & \text{for } \mathrm{Pr} \ge 3.0 \end{cases} \tag{12}$$

Other curve fits have occasionally been applied. For example, for $0.7 < \mathrm{Pr} < 10$: $G(\mathrm{Pr}) \approx 0.54\,\mathrm{Pr}^{0.37}$.

Equations (11) and (12) provide theoretical expressions for the stagnation-zone heat transfer coefficient for any value of B. They apply to either uniform wall temperature or uniform heat flux.

3. Laminar Stagnation Zone Nusselt Numbers

The laminar theory just described generally agrees well with experimental results when turbulence is eliminated; however, it must be emphasized that turbulence in the impinging jet has been reported to increase the heat transfer coefficient by 30–150% beyond that predicted in the following equations.

For high speed jets that are fully contracted, the nozzle-to-target separation has been shown experimentally to be unimportant. Nozzle-to-target separation can be expected to influence laminar jets if: (i) a sharp-edged nozzle is placed too close to the target to complete its contraction, so that a uniform profile is not achieved; (ii) if a tube nozzle is placed

far enough from the target that viscosity diffuses the parabolic profile toward uniform profile (at the bulk velocity); or (iii) if the jet velocity is low enough that gravitational acceleration causes significant variation in jet speed and size.

3.1 Uniform velocity-profile circular jets

For uniform velocity profile laminar jets, Liu et al. [5, 14] find

$$\mathrm{Nu}_d = 0.745\,\mathrm{Re}_d^{1/2}\mathrm{Pr}^{1/3} \tag{13}$$

This result is based on theory and on experiments with cold water. It should apply for all Reynolds numbers above 300–400 and for liquids with Prandtl numbers above 3 or so. The Nusselt number within 10% of the above value for $r/d < 0.7$; at larger radii, the heat transfer coefficient decreases rapidly. The theoretical lead constant is 0.813, but in the above equation it has been adjusted downward (by 9%) to bring it into close agreement with experimental data taken in the range $25,000 < \mathrm{Re}_d < 130,000$ using long cold water jets and sharp-edged orifice nozzles of 6.3 mm and 9.5 mm diameter. This equation was found to overpredict Nu_d for water jets of $d_j = 2.5$ mm by about 15%. A similar equation was given by Nakoryakov et al. [15] for high Prandtl number situations.

For nozzle-to-target separations of less than a few nozzle diameters, a sharp-edged orifice jet is not fully contracted, and the velocity profile is *not* uniform. In that case, heat transfer is likely to be higher than predicted here.

Little data is available for lower Reynolds numbers or for $\mathrm{Pr} < 1$ or $\mathrm{Pr} > 10$. For high Prandtl numbers, the above equation may be used. For Prandtl numbers near unity ($0.15 < \mathrm{Pr} < 3.0$), the theoretical results can be applied to obtain:

$$\mathrm{Nu}_d = 0.729\,\mathrm{Re}_d^{1/2}\mathrm{Pr}^{0.4} \tag{14}$$

For $\mathrm{Pr} \ll 1$, as for liquid metal jets, theory yields:

$$\mathrm{Nu}_d = 1.08\,\mathrm{Re}_d^{1/2}\mathrm{Pr}^{1/2} \tag{15}$$

Convective heat transfer coefficients for liquid metal jets are typically 3 to 8 times greater than those for water jets of the same diameter size and speed. Such jets may have value in applications for which very high h is required; for example, jets of liquid gallium have application to cooling high energy synchrotron x-ray components and particle accelerators [16, 17].

3.2 Parabolic velocity-profile circular jets

For jets issuing from tubes long enough to produce a fully developed laminar flow, the velocity profile is parabolic if the Reynolds number is below the transition value of 2000–4000. Theory and experimental data by Scholtz and Trass [11] show

$$\mathrm{Nu}_d = 1.648\,\mathrm{Re}_d^{1/2}\mathrm{Pr}^{0.361} \tag{16}$$

This equation should apply for $1 < \mathrm{Pr} < 10$ and Reynolds numbers ranging from 100–200 up to 2000–4000. This equation is in good agreement with sublimation experiments for $\mathrm{Pr} = 2.45$ and $500 < \mathrm{Re}_d < 1960$, and it appears to be unaffected by nozzle-to-target separation for $0.05 < l/d < 6$.[1]

The size of the uniform-h stagnation zone for this case is roughly $r/d < 0.15$, but the Nusselt number is within 10% of the stagnation-point value for $r/d < 0.4$; beyond this radius, the Nusselt number usually decreases sharply. An exception occurs when $l/d \leq 0.1$, for which case Nu_d can actually increase with r/d as the edge of the nozzle is approached.

4. Turbulent Jets

The manifolding and piping systems that supply liquid to nozzles are often turbulent, and unless the nozzle has a very high contraction ratio, this turbulence will be carried into the jet formed. A jet issuing from a fully developed tube flow without a terminating nozzle will also be turbulent if the Reynolds number is above about 4000. Turbulent jets have elevated heat transfer coefficients owing to both the direct effect of freestream turbulence on the boundary layer and the more indirect effect of a nonuniform velocity profile on the stagnation-point velocity gradient. The increases relative to laminar theory may range from 30% to 50%.

4.1 Velocity profile effects

In contrast to laminar velocity profiles, which typically vary from uniform to parabolic (with u_{max} up to $2u_f$), the velocity profiles of turbulent jets will likely vary between a uniform distribution and the mildly nonuniform distributions typical of turbulent pipe flows. In the latter case, however, the centerline velocity may still be significantly greater than the bulk velocity. For example, at a Reynolds number of 4000 in a circular tube, $u_{max}/u_f = 1.27$, and at $\mathrm{Re}_d = 10^5$, $u_{max}/u_f = 1.18$.

Stevens et al. [18] made laser-doppler measurements of the radial velocity gradient for several turbulent flow nozzles located a distance of one nozzle diameter from a target. For a contoured, converging nozzle, the gradient found was $B \approx 2.3$. This particular nozzle would be expected to have the most nearly uniform velocity profile, and its stagnation-point gradient is near the uniform-profile theoretical value of $B = 1.831$. On the basis of laminar theory, the difference in gradients would cause the contoured nozzle's Nusselt number to exceed that of a uniform profile by about 12%. Corresponding measurements for a fully developed pipe nozzle showed $B = 3.6$ at $l/d = 1$ [19], well above the uniform value; this difference would increase laminar heat transfer by 41%. One may conclude that variations in B among nozzles can have significant effects on turbulent jet heat transfer while the nozzle-to-target spacing is small.

[1] Submerged air jets between 19 and 51 mm diameter were used; l/d was small enough for these jets to behave as unsubmerged jets near the stagnation point.

However, all jets will approach a uniform velocity profile at the bulk velocity when l/d increases, because viscosity tends to eliminate radial gradients. Stevens and Webb [20] found bulk velocity was typically reached within about five diameters downstream of the nozzle. For long jets, one might infer that $B \to 1.83$ (uniform profile) and that the observed increases in heat transfer for long jets result from turbulence effects.

4.2 Turbulence effects

The stagnation-zone boundary layer is likely to remain laminar at the jet Reynolds numbers of interest, but turbulence in the impinging jet will tend to disrupt this very thin boundary layer, raising the heat transfer coefficient. This effect is very well documented for the stagnation zone of bodies in gas flows. For example, correlations for the stagnation-zone enhancement have been made [21, 22], and the effect has been clearly documented in gas-jet impingement [23], including time-resolved measurements of the turbulent heat flux [24]. This literature has been summarized by Vader et al. [25].

In contrast, few controlled studies of freestream turbulence are available for Prandtl numbers above unity (or well below unity), and no correlations or quantitative theory for freestream turbulence effects in those ranges of Pr are known to the author. Unfortunately, many applications of impinging liquid jets involve these Prandtl number ranges: general purpose cold-water jets with $2 < \mathrm{Pr} < 10$; fluorocarbon jets with $10 < \mathrm{Pr} < 70$ for electronics cooling; oil jets with $\mathrm{Pr} > 100$ for some electrical and machine-tool cooling applications; and liquid-gallium jets with $\mathrm{Pr} \approx 0.026$ for cooling accelerator or x-ray components.

Most turbulent liquid jet experiments are based on water jets with Prandtl numbers between 2.5 and 9. The associated correlations have usually fit data to the form suggested by laminar theory, adjusting the lead constant and Reynolds number exponent as necessary. The Prandtl number exponent is generally chosen on the basis of the laminar curve-fits to $G(\mathrm{Pr})$. Thus, the independent effects of freestream turbulence, Pr, and Re are lumped together in such results to produce simple engineering equations. In consequence, the available correlations for turbulent jet Nusselt number are likely to differ from design conditions if changes in the manifolding or nozzle arrangements increase or decrease the turbulence level relative to the experiments, or if the Prandtl number range is substantially different than the conditions of the experiments considered.

One well-defined turbulent nozzle is that of a fully developed turbulent pipe flow, as issues from a tube or channel of more than about 40 diameters in length. Turbulence intensities for such channel flows are generally 4 to 5% in the core of the flow; and extensive experimental and theoretical characterization is available [26]. Several investigators have adopted this nozzle as a standard for turbulent jets. Other nozzles may be less turbulent than this if they have a a strong and well-contoured contraction at the outlet; however, if a nozzle has flow separation within it, the turbulence level could be significantly higher than for a pipe nozzle.

4.3 Nusselt Numbers for Turbulent Jets

Circular jets issuing from long tubes will have fully developed turbulent flow for Reynolds numbers above a transition value of 2000–4000.

For $4000 < \mathrm{Re}_d < 52000$, Stevens and Webb [27] correlated

$$\mathrm{Nu}_d = 1.51\,\mathrm{Re}_d^{0.44}\mathrm{Pr}^{0.4}(l/d)^{-0.11} \tag{17}$$

to an average error of 15% and a maximum error of 60%. For $16600 < \mathrm{Re}_d < 43700$, Pan et al. [28] recommend the following correlation for nozzles whose stagnation-point velocity gradient is known:

$$\mathrm{Nu}_d = 0.49\,\mathrm{Re}_d^{1/2}\mathrm{Pr}^{0.4}B^{1/2} \tag{18}$$

These results are both based on cold water jets; the given Prandtl number exponents are assumed, but might be expected to apply in general range of 1 to 10. The stagnation zone, of constant Nu_d, is roughly $r/d < 0.7$. For a fully developed tube nozzle at $l/d = 1$, $B \approx 3.6$, and the second equation becomes

$$\mathrm{Nu}_d = 0.92\,\mathrm{Re}_d^{1/2}\mathrm{Pr}^{0.4} \tag{19}$$

for $16600 < \mathrm{Re}_d < 43700$ to an accuracy of about 5%.

At higher Reynolds number, both Gabour and Lienhard [29] and Faggiani and Grassi [30] report a stronger dependence of Nusselt number on Reynolds number. This may result from an increasing influence of freestream turbulence; however, further evidence is needed to verify that conjecture. For $25{,}000 < \mathrm{Re}_d < 85{,}000$, Gabour and Lienhard obtain

$$\mathrm{Nu}_d = 0.278\,\mathrm{Re}_d^{0.633}\mathrm{Pr}^{1/3} \tag{20}$$

based on experiments with cold water jets having $8.2 < \mathrm{Pr} < 9.1$ and tube diameters between 4.4 and 9.0 mm. The uncertainty of the data (at a 95% confidence level) is less than $\pm 10\%$. Gabour found that the effect of changing l/d between 1 and 20 was within the uncertainty of the data. The assumed Prandtl number exponent is appropriate for $\mathrm{Pr} > 3$.

Figure 5 shows the stagnation-zone Nusselt number of jets froms from fully developed tube nozzles for $500 < \mathrm{Re}_d < 10^5$ and $\mathrm{Pr} = 8$, as predicted by Eqs. (16), (17), and (20). (Eq. 19 is quite close to those shown, and l/d was set to 1 in Eq. 17). The Nusselt number for a sharp-edged orifice nozzle (Eq. 13) is also shown.

For liquid metal jets, the impact of turbulence may be expected to be small, owing to the high molecular conductivity relative to the turbulent eddy diffusivity. Lienhard [12] suggested the use of the laminar flow result, Eq. 15, for such situations. This conjecture was recently confirmed experimentally by Silverman and Yarin [31] for turbulent gallium jets in the range $40{,}000 < \mathrm{Re}_d < 110{,}000$.

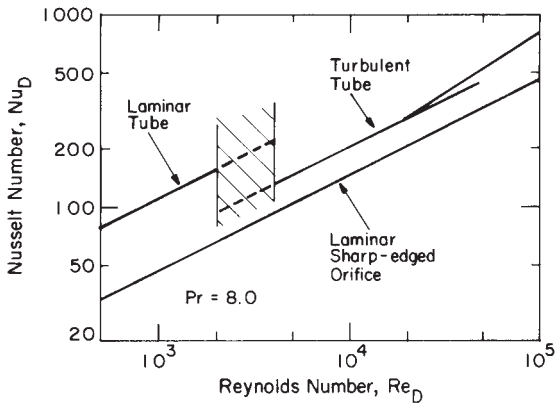

Figure 5: Stagnation-zone Nusselt number for circular liquid jets at Pr = 8.

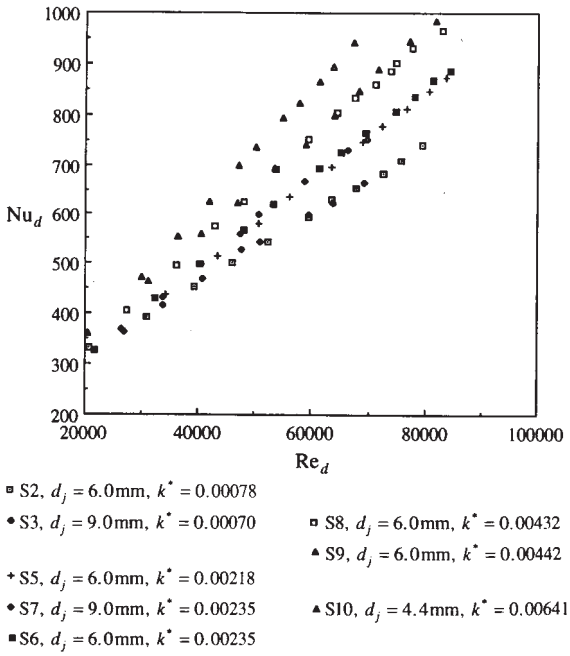

Figure 6: Wall roughness effects on stagnation-zone Nusselt number for circular turbulent liquid jets at Pr = 8–9 (data from [29]).

4.4 Jets Impinging on Rough Walls

The very thin boundary layer of the stagnation zone can be disrupted by even small levels of wall roughness. Gabour and Lienhard [29] measured the stagnation-point Nusselt number for fully developed turbulent cold-water jets impinging on surfaces of varying roughness. They found that roughness of only 28 μm rms height could raise the Nusselt number by up to 50%.

For those experiments, mild steel (1010) surfaces were scored in a cross-hatch pattern. The depth of scoring was varied to yield a range of rms roughness, $4.7 \leq k \leq 28.2$ μm, while holding the pattern of roughness fixed. Measurements were made for nozzles of diameter d = 4.4, 6.0 and 9.0 mm and Reynolds numbers from 20,000 to 84,000. The Prandtl number was held between 8.2 and 9.1. Roughness effects on the Nusselt number depended on Re_d and the dimensionless roughness $k^* = k/d$, as shown in Fig. 6. On these figures, the lowest curves ($k^* < 0.0008$) are effectively smooth walls; for higher k^*, the Nusselt number is greater than for a smooth surface, and the enhancement rises with Re_d.

Gabour and Lienhard constructed a curve fit for the threshold level of roughness at which the Nusselt number is increased by 10%:

$$k^* = 5.95\,\mathrm{Re}_d^{-0.713} \tag{21}$$

For lower levels of roughness (smaller k^*), the surface can be viewed as smooth. Data for other values of Pr are not available, but jets of higher Pr liquids would be expected to be more susceptible to wall roughness effects, owing to the thinner thermal boundary layer.

The overall scaling of stagnation-point wall roughness is different than for standard turbulent boundary layers, owing to the nearly zero shear stress of the stagnation zone, and this scaling is as yet not known.

5. Local Heat Transfer Downstream

The flow downstream of the stagnation zone is characterized by growing boundary layers and a decreasing heat transfer coefficient. The boundary layers are laminar near the stagnation zone and undergo a turbulent transition further downstream. Transition produces a local increase in the heat transfer coefficient, again followed by a declining trend. If the incoming jet is turbulent, local h upstream of transition can be increased, especially in the accelerating flow near the stagnation zone; and the location of turbulent transition is moved upstream.

Axisymmetric jets spread thinner as they travel radially outward (Fig. 7). The flow perimeter increases as $2\pi r$, and inviscid mass conservation requires the liquid sheet thickness to decrease as $h(r) = d^2/8r$. This rapid decrease quickly brings the growing boundary layer into contact with the surface of the liquid sheet, transforming the flow from a boundary layer into a high-momentum viscous film with a radially increasing bulk temperature. Thus, analysis and correlation of circular jet heat transfer becomes complicated, owing to radial changes in the heat transfer mechanism. In addition, any incoming turbulence in the jet can greatly disturb the free surface of the thin liquid sheet, causing splattering of the liquid and a very rapid transition to a turbulent film flow.

5.1 Flow field

A laminar axisymmetric jet creates a radial film that evolves as shown in Fig. 7. The thickness of the liquid sheet initially decreases with radius (as $1/r$), but, because viscous drag slows the liquid sheet, its thickness begins to increase at larger radii. The flow field may be divided into successive regions:

1. *The stagnation zone.*
2. *The laminar boundary layer region*, in which the viscous boundary layer thickness, δ, is less

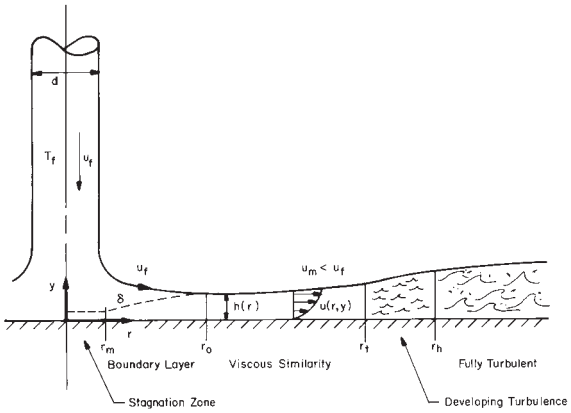

Figure 7: Downstream development of an axisymmetric impinging jet.

than the liquid sheet's thickness, $h(r)$, and the rest of the liquid sheet moves at the incoming jet's speed, u_f, and nearly parallel to the wall.

3. *The viscous similarity region*, in which viscous effects extend through the entire liquid film [$\delta = h(r)$]. In this region, the surface speed, u_m, decreases with increasing radius.

4. *The region of developing turbulence.*

5. *The region of fully turbulent flow.* This region may relaminarize farther downstream, as the film speed decreases.

Theoretical solutions for the boundary layer and viscous similarity region were first obtained by Watson [32]. Watson's analysis of the boundary layer region led to a Blasius type similarity solution for $\delta < h(r)$. In the region where $\delta = h(r)$, Watson obtained an elegant similarity solution that encompasses the entire thickness of the liquid sheet. Watson also obtained solutions for a turbulent film flow and for the hydraulic jump; however, these solutions are somewhat unsatifactory, as discussed by Liu et al. [14] and by Liu and Lienhard [33]. Watson's laminar results were experimentally substantiated by Azuma and Hoshino [34, 35, 36, 37] using laser-doppler measurements. Sharan [38] independently obtained approximate integral-method solutions for both regions, and Wang et al. [39] developed a series solution for the boundary layer region.

The various analytical studies are in relatively good agreement with one another, in spite of minor differences in the approximations they employ. To reasonable accuracy, the integral-method results can be used [14, 38, 40], as we now summarize.

The region of boundary layer behavior, with $u_m(r) = u_f$, begins at $r \approx 2.23\,d$. In this region, the boundary layer thickness is approximately

$$\delta = 2.679\left(\frac{rd}{\mathrm{Re}_d}\right)^{1/2} \tag{22}$$

and the velocity profile is approximately:

$$u(r,y) = u_m(r)\left[\frac{3}{2}\frac{y}{\delta} - \frac{1}{2}\left(\frac{y}{\delta}\right)^3\right] \tag{23}$$

The viscous boundary layer reaches the surface of the liquid sheet at a radius r_o given by:

$$r_o = 0.1773\,\mathrm{Re}_d^{1/3} d \tag{24}$$

Beyond r_o, the free surface speed decreases as:

$$u_m(r) = \frac{1}{5}\frac{u_f\, d^2}{h(r)\, r} \tag{25}$$

where the liquid sheet thickness is

$$h(r) = 0.1713\left(\frac{d^2}{r}\right) + \frac{5.147}{\mathrm{Re}_d}\left(\frac{r^2}{d}\right) \tag{26}$$

For $r > r_o$, the velocity profile may be obtained from the polynomial approximation (Eq. 23) with u_m from Eq. (25) and $\delta = h(r)$ from Eq. (26).

The radius of onset of turbulence, r_t, was correlated by Liu et al. [14] as

$$\frac{r_t}{d} = 1200\,\mathrm{Re}_d^{-0.422} \tag{27}$$

Liu et al. inferred from heat transfer data the radius at which turbulence became fully developed, and correlated it as:

$$\frac{r_h}{d} = 28600\,\mathrm{Re}_d^{-0.68} \tag{28}$$

In the fully turbulent region, Azuma and Hoshino [36] found that a 1/7th power velocity distribution worked well. The skin friction coefficient there can be approximated as [14]

$$C_f = 0.073\left(\frac{r}{d\,\mathrm{Re}_d}\right)^{1/4} \tag{29}$$

and the film thickness may be estimated as

$$\frac{h(r)}{d} = \frac{0.02091}{\mathrm{Re}_d^{1/4}}\left(\frac{r}{d}\right)^{5/4} + C\left(\frac{d}{r}\right) \tag{30}$$

with

$$C = 0.1713 + \frac{5.147}{\mathrm{Re}_d}\frac{r_t}{d} - \frac{0.02091}{\mathrm{Re}_d^{1/4}}\left(\frac{r_t}{d}\right)^{1/4} \tag{31}$$

5.2 Heat transfer

Existing analytical solutions for heat transfer assume negligible heat transfer from the liquid surface; in particular, evaporation is neglected. This situation should prevail for a surface temperature, T_{sf}, that remains relatively low. If evaporation from the free surface becomes important, the theoretical expressions for the Nusselt number will underpredict.

Heat transfer in the downstream region has been modelled by various investigators, including Chaudhury [41], Nakaryakov et al. [15], Liu and Lienhard

[40], Wang et al. [39], and Liu et al. [14]. Chaudhury used Watson's laminar velocity profiles to obtain similarity solutions for the liquid temperature field along a uniform temperature wall. Wang et al. developed solutions in the boundary layer region ($r < r_o$) that apply to arbitrary distributions of wall temperature and heat flux. Nakaryakov et al. [15] provide theoretical and experimental mass transfer results that are analogous to uniform wall temperature and very high Prandtl number, based on a linear approximation to the velocity profile within the concentration boundary layer.

Most experimental data for downstream heat transfer are for uniform wall heat flux, and this case has been modelled by Liu and Lienhard [40] and by Liu et al. [14]. Liu and Lienhard separated the laminar flow into several thermal regions for $\mathrm{Pr} > 1$:

Region 1. *The stagnation zone.*

Region 2. $\delta < h$ *region*: The thermal and viscous boundary layers do not reach the surface; surface temperature and velocity, T_{sf} and u_m, equal inlet temperature and velocity, T_f and u_f.

Region 3. $\delta = h$ *and* $\delta_t < h$ *region*: The viscous boundary layer has reached the free surface. The velocity outside the viscous boundary layer decreases with radius, but the surface temperature remains at the inlet temperature, T_f.

Region 4. $\delta = h, \delta_t = h$, *and* $T_w < T_{sat}$ *region*: In this region, the thermal boundary layer has reached the surface. The surface temperature increases with radius.

In the laminar regions, Liu and Lienhard applied the integral energy equation

$$\frac{d}{dr}\int_0^{\delta_t} ru(T - T_f)\,dy = \frac{q_w}{\rho c_p}\,r \tag{32}$$

where $T = T(r, y)$ is the liquid temperature profile. In region 2 (before the thermal boundary layer reaches the surface), they approximated the velocity profile as Eq. (23) and the temperature profile as

$$T(r,y) - T_w = (T_f - T_w)\left[\frac{3}{2}\frac{y}{\delta_t} - \frac{1}{2}\left(\frac{y}{\delta_t}\right)^3\right] \tag{33}$$

for T_w the wall temperature, which increases with radius. While $r < r_o$, the integral solution for the local heat transfer coefficient in the boundary layer region is approximately equal to

$$\mathrm{Nu}_d = 0.632\,\mathrm{Re}_d^{1/2}\mathrm{Pr}^{1/3}\left(\frac{d}{r}\right)^{1/2} \tag{34}$$

which shows the local heat transfer coefficient to decrease as $1/\sqrt{r}$.

Region 2 ends and region 3 begins where the viscous boundary layer reaches the film surface at r_o. In region 3, the integral solution is:

$$\mathrm{Nu}_d = \frac{0.407\,\mathrm{Re}_d^{1/3}\mathrm{Pr}^{1/3}\,(d/r)^{2/3}}{[0.1713(d/r)^2 + (5.147\,r/\mathrm{Re}_d\,d)]^{2/3}\left[\frac{1}{2}\left(\frac{r}{d}\right)^2 + C_3\right]^{1/3}} \tag{35}$$

where

$$C_3 = \frac{0.267(d/r_0)^{1/2}}{\left[0.1713\,(d/r_0)^2 + (5.147\,r_0/\mathrm{Re}_d\,d)\right]^2} - \frac{1}{2}\left(\frac{r_0}{d}\right)^2 \tag{36}$$

Region 3 ends and region 4 begins where the thermal boundary layer reaches the liquid surface at $r = r_1$; equations defining r_1 are given by Liu and Lienhard [40]. In region 4:

$$\mathrm{Nu}_d = \frac{0.25}{\frac{1}{\mathrm{PrRe}_d}\left[1 - \left(\frac{r_1}{r}\right)^2\right]\left(\frac{r}{d}\right)^2 + 0.130\,\frac{h(r)}{d} + 0.0371\,\frac{h(r_1)}{d}} \tag{37}$$

where $h(r)$ is given by Eq. (26) above.

Region 4 will occur only for Pr less than a critical value near five[2]; otherwise, the thermal boundary layer does not grow fast enough to reach the surface of the liquid film, which thickens with increasing radius owing to viscous retardation. Liu et al. found that the predictions for regions 3 and 4 are within a few percent of each other, and they suggest that the prediction of region 3 be used for any Pr above unity. Regions 3 and 4 correspond to Watson's self-similar viscous flow regime.

Liu et al. estimated the fully turbulent heat transfer using the thermal law of the wall, from which, using Eq. (29, 30), the Nusselt number is

$$\mathrm{Nu}_d = \frac{q_w\,d}{k(T_w - T_f)} = \frac{8\,\mathrm{Re}_d\mathrm{Pr}\,f(C_f,\mathrm{Pr})}{49\,(hr/d^2) + 28\,(r/d)^2\,f(C_f,\mathrm{Pr})} \tag{38}$$

In this equation,

$$f(C_f,\mathrm{Pr}) = \frac{C_f/2}{1.07 + 12.7(\mathrm{Pr}^{2/3} - 1)\sqrt{C_f/2}} \tag{39}$$

When Pr is well above unity, this simplifies to

$$\mathrm{Nu}_d = 0.0052\,\mathrm{Re}_d^{3/4}\left(\frac{d}{h}\right)\left(\frac{d}{r}\right)^{3/4} \times \left(\frac{\mathrm{Pr}}{1.07 + 12.7(\mathrm{Pr}^{2/3} - 1)\sqrt{C_f/2}}\right) \tag{40}$$

Comparison of these equations to experimental data for a uniform profile laminar jet [14] is shown in Fig. 8, and agreement is seen to be very good. Liu et al. also give integral solutions for $\mathrm{Pr} < 1$.

[2] Liu and Lienhard [40] gave this value as 4.86. If the higher-order terms in the integral analysis are retained, the value becomes 5.23.

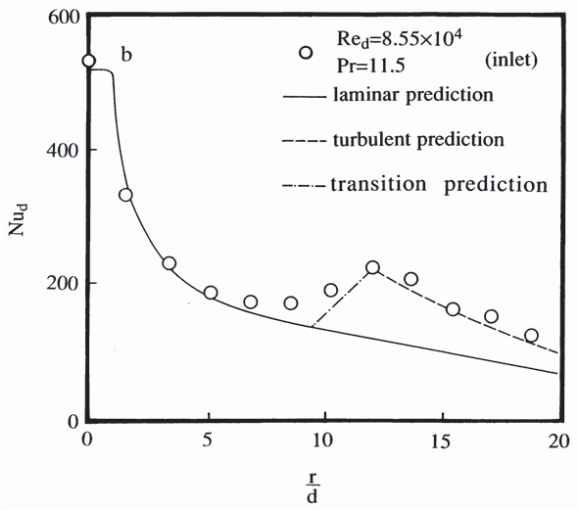

Figure 8: Comparison of laminar theory to data [14].

The theoretical solutions should be evaluated using liquid properties at the local liquid temperature (averaged across the liquid thickness). In particular, the liquid viscosity varies strongly with temperature for most liquids and may decrease significantly with radius. To use these results in calculating Nu_d and $T_w(r)$, a numerical integration in the radial direction is most expedient [40].

6. Splattering Jets

Turbulence in an axisymmetric jet is carried into the radially spreading liquid film, where it has two primary effects. First, the turbulence tends to increase convective heat transfer in the boundary layer downstream of the stagnation zone and tends to promote turbulent transition of the thin liquid sheet. The turbulent sheet has greater skin friction than a laminar sheet: Measurements of nonsplattering turbulent jets [20] show that the liquid surface speed begins to drop at $r \approx 2.5d$, sooner than predicted by laminar flow theory.

The second effect of jet turbulence is to disturb the surface of the incoming jet. These disturbances are carried into the thinning liquid sheet, where the radial spreading can produce a strong increase in their amplitude. If the initial disturbances are large enough, the amplified disturbances can cause droplets to break free from the liquid sheet, resulting in splattering (Fig. 9).

Splattering is more important when the jets are longer and have a higher Weber number, because the disturbances reaching the sheet are then larger. Strong splattering can result in atomization of 30 to 70% of the incoming liquid (Fig. 10), and because the airborne droplets no longer contribute to cooling the wall, heat transfer far downstream is degraded. On the other hand, splattering has no independent influence on heat transfer in the stagnation region, because the droplets break away several diameters downstream of it.

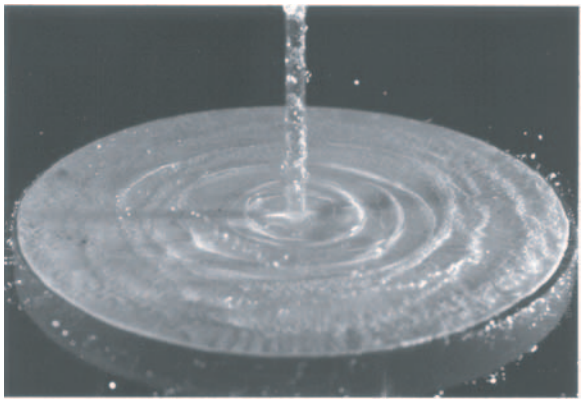

Figure 9: Splattering turbulent jet showing radially travelling waves: $\mathrm{Re}_d = 28,000$, $\xi = 0.11$, fully developed tube nozzle.

Figure 10: Splattering turbulent jet: $\mathrm{Re}_d = 48,300$, $\xi = 0.31$, fully developed tube nozzle.

6.1 The mechanics of splattering

Initial studies of splattering, by Errico [42] and by Lienhard et al. [43], demonstrated that it is driven by the disturbances on the surface of the impinging jet. Thus, undisturbed laminar jets do not splatter, unless they are long enough to have significant capillary instability. Turbulent jets, on the other hand, develop surface roughness as a result of liquid-side turbulent pressure fluctuations, and they are highly susceptible to splattering.

Errico [42] induced splattering for laminar jets by creating surface disturbances with a fluctuating electric field; these disturbances were carried, as radial waves, into the liquid film, causing splatter downstream. When a turbulent jet strikes a target, similar travelling waves originate near the impingement point and travel outward on the film (see Fig. 9). When the jet disturbances are sufficiently large, these waves sharpen and break into droplets. All observations indicate that the amplitude of the disturbances on the jet governs splattering. They further indicate that splattering is a non-linear instability phenomenon, since the liquid film is clearly stable to small disturbances but unstable to large ones [44].

Once droplets break away from the liquid sheet, they remain airborne. Lienhard et al. [43] made

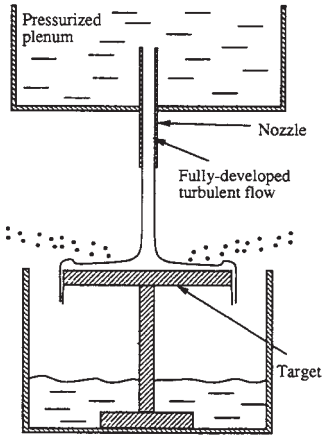

Figure 11: Measurement of the splattered flow rate.

phase-doppler measurements of the size and speed of the departing droplets and found that the droplets travel at a low angle with nearly the speed of the incoming jet; thus, they do not fall back into the liquid film at an appreciable rate. Their measurements, and stroboscopic observations by Errico [42], show that droplets leave the liquid sheet within a fairly narrow radial band. The radius of departure was estimated to be $r/d \approx 4.5$.

6.2 The fraction of liquid splattered

Measurements of the splattered liquid flow rate for fully turbulent turbulent jets were first reported by Lienhard et al. [43] in the form of the ratio of splattered flow rate, Q_s, to the incoming flow rate, Q (Fig. 11):

$$\xi = \frac{Q_s}{Q} \tag{41}$$

This quantity is easily measured by capturing the unsplattered liquid and determining its flow rate. Lienhard et al. also proposed that splattering depends primarily on the rms amplitude of jet surface disturbances. In this model, turbulent pressure fluctuation in the bulk liquid jet create the initial surface disturbances near the nozzle outlet, which then grow in the streamwise direction.

The growth of the surface disturbances depends on l/d and the jet Weber number,

$$\mathrm{We}_d = \rho u_f^2 d/\sigma. \tag{42}$$

In Fig. 12, the amount of splattering, ξ, is shown as a function of nozzle-to-target separation, l/d, for several nozzle diameters and Reynolds numbers [45]. Each solid line represents data for a narrow range of Weber numbers, varying by less than $\pm 3\%$ around the stated mean value, a range equal to the experimental uncertainty of We_d. As the figure shows, for constant We_d, ξ is a function of l/d; different curves are obtained for different Weber numbers, with splattering increasing as the Weber number increases.

To study the effect of surface tension directly, a solution of approximately 10% by volume of isopropanol in water was used, having $\sigma = 0.042$ N/m

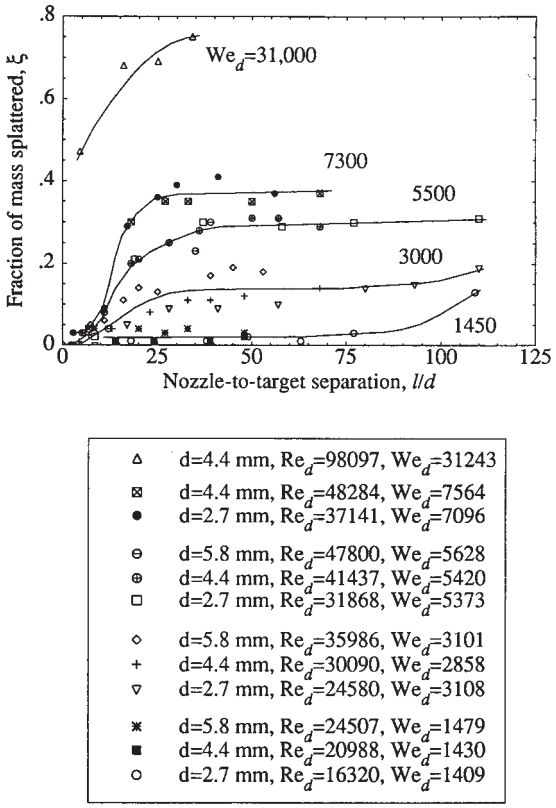

Figure 12: Splatter as a function of l/d and We_d [45].

(versus 0.072 N/m for pure water). These data show good agreement with data for water when scaled with the Weber number (Fig. 13). Splattering increases as surface tension decreases.

At any given Weber number and nozzle-target separation, the splatter fraction, ξ, depends extremely weakly on the Reynolds number, if at all. For example, in the data set for $\mathrm{We}_d = 5500$, the Reynolds number increases by a factor of 1.5 without any discernible change in the splatter fraction, ξ. In contrast, a factor of 1.3 increase in the Weber number (from 5500 to 7300) produces significant increase in the splatter fraction (roughly +25%).

An influence of Reynolds number would be expected to arise primarily from viscous effects near solid boundaries, either in setting the pipe nozzle's turbulence intensity or as an influence of the viscous boundary layer along the target. The stagnation-point boundary layer is extremely thin relative to the liquid layer, and thus it may have little effect on the surface waves near the region of impingement. The pipe-turbulence variation maybe quantified by observing that the ratio of rms turbulent speed to friction velocity, u'/u_*, is nearly independent of Reynolds number in fully developed turbulent pipe-flows [45]. Therefore, upon using the definition, $u_* = u_f\sqrt{f/8}$, and the Blasius friction factor equation ($f = 0.316\mathrm{Re}_d^{-1/4}$ for $4000 < \mathrm{Re}_d < 10^5$), one finds

$$\frac{u'}{u_f} \propto \frac{u_*}{u_f} \propto \sqrt{f} \propto \mathrm{Re}_d^{-1/8}$$

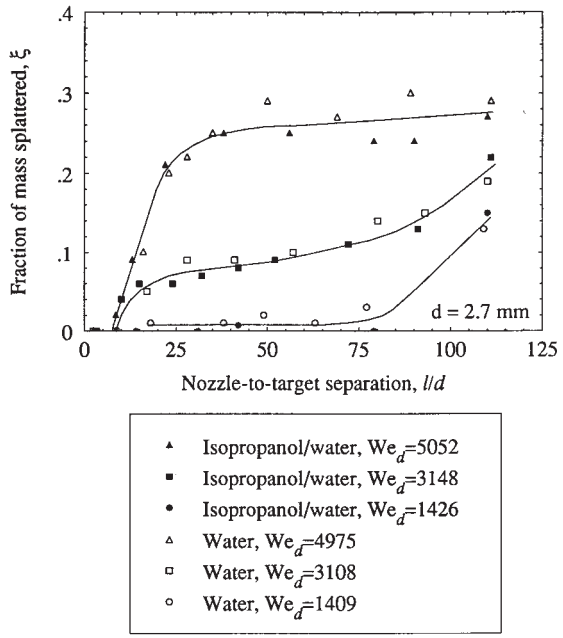

Figure 13: Splattering as a function l/d and We_d for liquids of different surface tension [45].

This weak dependence of the turbulence intensity on the Reynolds number may explain the lack of any significant dependence of splattering on Re_d.

6.3 The relation of splattering to jet surface disturbances

Referring to Figs. 12 and 13, we see that very little splattering occurs close to the jet exit (small l/d), typically less than 5%. Beyond this region, the amount of splattering at first increases with distance, l/d. Farther downstream, it reaches a plateau. To explain these observations we may refer to direct measurements of the amplitude of turbulent liquid jet surface disturbances.

Bhunia and Lienhard [46] used a laser-sheet and high frequency-response photodiode to measure the instantaneous diameter of turbulent liquid jets (Fig. 14). They obtained the rms amplitude of jet surface disturbances, δ_{rms}, at different axial locations along jets of various Weber numbers (Fig. 15). Starting from nearly zero near the nozzle exit, δ_{rms} initially grows rapidly as the jet moves downstream; farther downstream the growth rate diminishes and the rms disturbance tends to an asymptotic limit. The dependence of δ_{rms}/d of jet Weber number is also apparent.

This growth of disturbances is the probable cause of the increase in the splatter fraction as the nozzle-to-target separation is increased. The steadily decreasing rate of amplitude growth results in a plateau of the disturbance amplitude which corresponds to that in the splatter fraction data.

Direct comparison of the measurements of δ_{rms} to data for ξ and shows a reasonable correlation between the size of δ_{rms} and the fraction of liquid splattered (Fig. 16). This graph was obtained by plotting previously measured splatter fraction ξ values

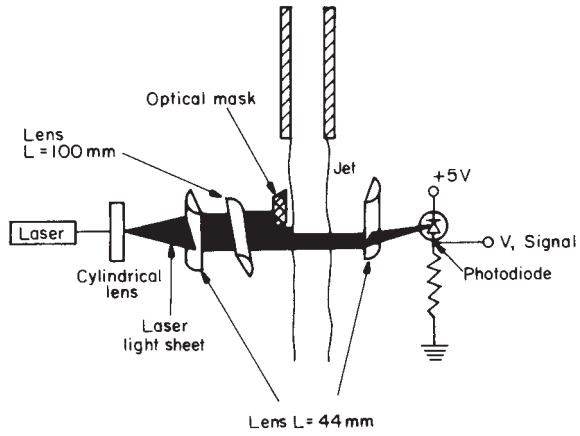

Figure 14: Laser sheet measurement of jet surface roughness [46].

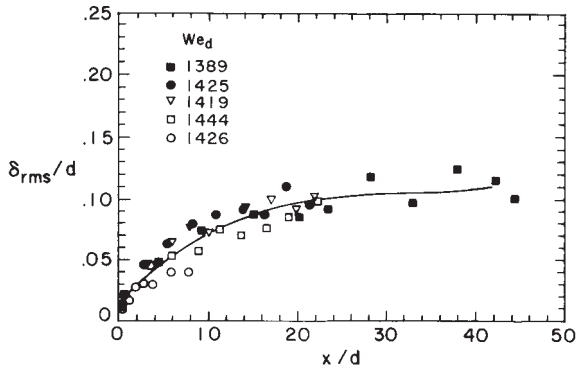

Figure 15: Root-mean-square surface roughness data: several runs at fixed Weber number, showing variability of data [46].

against δ_{rms}/d for jets of the same Weber number and $l/d = x/d$ [46]. Each set of data for a given nozzle diameter and jet Weber number consists of measurements at several different axial locations, x/d. The correlation is reasonably clear, given that both ξ and δ_{rms} have significant variability, and it provides further evidence that splattering is due to surface disturbances on the jets and is governed by the amplitudes of those disturbances.

For very long, low We_d jets the plateau of splattering ends, and ξ again increases with l/d (Fig. 13). This may reflect the appearance of ordinary capillary instability on these jets, which have relatively little turbulence-generated surface roughness.

6.4 The onset of splattering

Bhunia and Lienhard [45] defined the onset of splattering as the point where 5% of the incoming fluid is splattered. For a jet of a given Weber number, the onset point is reached at a certain l/d, denoted as l_o/d. A correlation for the onset point data is

$$\frac{l_o}{d} = \frac{130}{1 + 5 \times 10^{-7}\,\mathrm{We}_d^2} \tag{43}$$

For low Weber numbers, near 100, turbulent disturbances are strongly damped by surface tension,

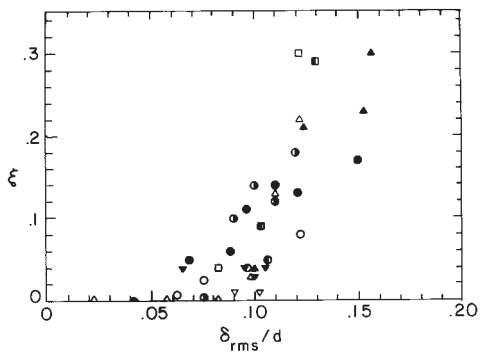

Fluid	d (mm)	We_d
◐ Isopropanol / Water	5.8	3200
▲ Water	5.8	5500
●		3120
▼		1450
□ Water	4.4	7535
△		5290
○		2850
▽		1400
◙ Water	2.7	7000
◐		3175

Figure 16: Splatter fraction as a function of rms surface roughness [46].

and the observed onset lengths are actually rather close to the capillary breakup lengths. In this range, splattering is essentially of drop impingement type.

6.5 The influence of surfactants on splattering

Surfactants lower surface tension by forming a surface adsorbed monolayer at the liquid surface. When a new liquid surface is formed, some time is required for surfactant molecules to diffuse to the surface in sufficient concentration to alter the surface tension. To study the role of surfactants in splattering, Bhunia and Lienhard [45] used a mixture of approximately 0.2% detergent in water. This reduced the surface tension of the static solution (liquid surface at rest) to 0.027 N/m and corresponded to a saturated concentration of surfactant. They found that the splatter fraction for the surfactant-laden jet is identical to that for a pure-water jet of the same velocity, diameter, and length; in fact, if We_d for the surfactant jet is calculated on the basis of pure-water surface tension, the curves for the surfactant jets are identical to those of the pure jets. From the standpoint of splattering, the surface tension of the surfactant jet is effectively the surface tension of the pure liquid.

To further explore this behavior, Bhunia and Lienhard [46] measured the surface-roughness evolution of jets containing surfactant. They found that the surface roughness of a surfactant-laden jet evolved at the same rate as for a pure-water jet of the same size and speed. In other words, surfactants do not decrease the stability of the turbulent jet surface under conditions like these.

A possible cause of this behavior is the finite time required to establish a saturated concentration of

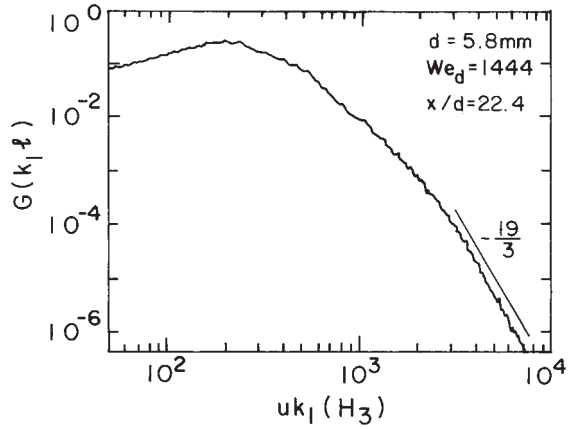

Figure 17: Measured power spectra of turbulent liquid-jet surface disturbances. Ordinate is proportional to $G(k_1 l)$ [46].

surfactant on the jet surface. Inside the nozzle, the surfactant is in the bulk of the liquid. When the liquid exits the nozzle, a new free surface is formed which is not initially saturated with surfactant. During the time needed for the surfactant to diffuse from the bulk to the free surface, the surface remains unsaturated, and in this initial length of the jet, the surface tension remains near that of pure water.

6.6 Power spectra of surface disturbances

Figure 17 shows the wavenumber spectrum of jet-surface disturbances. The ordinate is proportional to the power spectrum of the free surface disturbance amplitude, $G(k_1 l)$ [see Eq. (46) below], and the abscissa is uk_1, where k_1 is the wavenumber in the direction of the jet axis, u is the free surface velocity, and l is the integral scale of turbulence.

These graphs of power spectrum versus disturbance wavenumber show that broadband turbulent disturbances dominate over any single wavenumber disturbance related to a Rayleigh-type instability. In addition, these log-log spectral plots show a portion of very nearly linear decrease in the spectral amplitude, characteristic of high wavenumber turbulence [47]. Except for measurement locations very near the nozzle, the slope of this linear portion is $-19/3$, so that the spectra decay as $k_1^{-19/3}$.

A model that explains the spectral decay was constructed by Bhunia and Lienhard [46], who approximated the jet surface as planar. The liquid pressure fluctuations near the free surface are balanced by the surface tension (Fig. 18), so that the Young-Laplace equation applies along the plane of the surface

$$p = -\sigma \left(\frac{\partial^2 \delta}{\partial x^2} + \frac{\partial^2 \delta}{\partial y^2} \right) \tag{44}$$

Bhunia and Lienhard modelled the liquid-side pressure fluctuations as those of a spatially homogeneous turbulence. By treating both p and δ as stationary random functions [48], they obtained the following equation for the mean-squared amplitude of surface

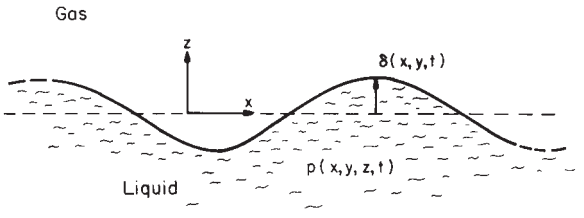

Figure 18: Liquid-jet surface displacement in response to pressure fluctuation.

disturbances:

$$\overline{\delta^2} = \int_{-\infty}^{\infty}\int_{-\infty}^{\infty} \frac{1}{\sigma^2(k_1^2+k_2^2)^2} \int_{-\infty}^{\infty} F(k)dk_3dk_2dk_1 \tag{45}$$

Here, $F(k)$ is the turbulent pressure spectrum, and (k_1, k_2, k_3) are the (x, y, z) components of a wavevector of magnitude k. For isotropic, homogeneous turbulence [49],

$$F(k) \sim 0.26\rho^2 u'^4 l^3 (kl)^{-13/3}, \qquad kl \gg 1$$

where u' is the rms turbulent velocity and l is the integral scale of turbulence.

To relate these results to the measured one dimensional spectrum of the surface disturbances, $G(\eta)$, they introduced the definition

$$\frac{\overline{\delta^2}}{l^2} = \int_0^{\infty} G(\eta)d\eta \tag{46}$$

where η is the wavenumber of the free surface disturbances nondimensionalized with the integral scale of turbulence, l. From Eqs. (45) and (46), it follows that at high wavenumbers ($\eta \gg 1$) the disturbance spectrum is

$$G(\eta) \sim 0.26 \times 2\pi \frac{\rho^2 u'^4}{\sigma^2} \frac{l^{-13/3}}{k_p^3} \int_{-\infty}^{\infty} \frac{dk_3}{(k_p^2+k_3^2)^{13/6}} \tag{47}$$

where we have transformed from Cartesian to polar coordinates in the wavenumber plane, $(k_1, k_2) \rightarrow (k_p, \theta)$, with $\eta = k_p l$ and $k_p = \sqrt{k_1^2 + k_2^2}$. Upon evaluating the integral, the one-dimensional spectrum of free surface turbulent disturbances (measured along any direction θ) is found to be

$$G(\eta) \sim 2.41 \left(\frac{\rho^2 u'^4 l^2}{\sigma^2}\right) \eta^{-19/3}, \qquad \eta \gg 1 \tag{48}$$

This analysis explains the observed $-19/3$ slope in the log-log plots of the disturbance spectra as a consequence of the $k_1^{-7/3}$ variation of the one-dimensional spectrum of the pressure fluctuations and a factor of k_1^{-4} introduced by the derivatives of δ in the capillary force balance equation.

7. High Heat Flux Jet Arrays

Impinging liquid jets, with their very high heat transfer coefficients, have proven to be quite effective for high heat flux cooling. When heat transfer is confined to the stagnation region of a jet, a high heat transfer coefficient may be combined with a high stagnation pressure, which raises the liquid saturation temperature and facilitates non-boiling heat removal. Liu and Lienhard [50] used high speed water jets to remove fluxes as high as 400 MW/m^2 over small areas. To obtain high fluxes over larger areas, jet arrays have proven to be useful. Oh et al. [51] and Lienhard and Hadeler [52] used an array of fourteen 2.78 mm ID nozzles on 10 mm centers to produce 47 m/s water jets impinging on an area of 10 cm^2. In experimental tests, the jet array removed fluxes of up to 17 MW/m^2 by forced convection alone; the associated heat transfer coefficient was measured to be 220 kW/m^2.

Two practical difficulties arise in experimentation with jets at such high heat fluxes. The first is that the solid surfaces involved experience very high temperature gradients, and the associated thermal stresses are sufficient to induce yielding of the metal [53]. In the jet array experiments, dispersion-strengthened copper plates (alloy C15315) formed the heat transfer surface; these metal-matrix materials have the strength of stainless steel at high temperature while retaining most of the thermal conductivity of copper. The second difficulty is to provide test heating at such high fluxes. Heating for these experiments was produced using 75 μm thick vacuum-plasma-sprayed Ni-80/Cr-20 electrical resistance heaters formed directly on the heat transfer surface [54]. These heaters were driven at nearly 1000 A and 24 Vdc. The development of these heaters required substantial effort, and the technology has attracted some interest in its own right.

8. Concluding Remarks

Liquid jet impingement remains a rich source of problems having both practical value and academic interest. Relatively simple experiments are possible, as is theoretical analysis using either classical or modern techniques.

The work summarized above points to a number of open questions. The spectral analysis of turbulent surface disturbances has not been fully explored. Theory remains to be developed, and additional experiments can easily be done using inexpensive optical equipment together with computer-aided data acquisition. The role of wall roughness in the stagnation zone warrants significantly more study. Additional experimentation is required, and theory for scaling roughness effects is needed. Small diameter laminar jets have shown deviations from theory in a number of experiments, whereas larger jets track theory well. This remains to be explained. Further work on splattering is needed, for example, in the sense of quantifying the downstream mechanisms. A theory of turbulent jet heat transfer remains missing, if only for the stagnation zone; existing results are essentially correlations built from laminar theory.

The research on jets in our lab was, of course, largely carried out by the many students who have

worked with me over the years. I wish to thank all of them for their efforts and insights, and I particularly wish to acknowledge the contributions of Dr. Xin Liu, Dr. Sourav K. Bhunia, and Dr. Laurette A. Gabour.

References

[1] K. Hiemenz, Die Grenzschicht an einem in den gleichformigen Flussigkeitsstrom eingetauchten geraden Kreiszylinder, Dingler's Polytech. J. **326**, 321, 1911.

[2] F. Homann, Der Einfluss grosser Zahigkeit bei der Strommung um den Zylinder und um die Kugel, Z. Angew. Math. Mech. **16**, 153-164, 1936.

[3] L. Howarth, The Boundary Layer in a Three-Dimensional Flow—Part II. The Flow Near a Stagnation Point, Phil. Mag., Series 7, **42**, 1433–1440, 1951.

[4] G.K. Batchelor, Fluid Dynamics, pg. 105, Cambridge UK, Cambridge University Press, 1967.

[5] X. Liu, L.A. Gabour, and J.H. Lienhard V, Stagnation Point Heat Transfer During Impingement of Laminar Liquid Jets: Analysis with Surface Tension, J. Heat Trans. **115**(1), 99–105, 1993.

[6] G. Birkhoff and E. H. Zarantonello, Jets, Wakes, and Cavities, pp. 229–231 New York, Academic Press, 1957.

[7] W. Schach, Umlenkung eines freien Flussigkeitsstrahles an einer ebenen Platte, Ing.-Arch. **5**, 245–265, 1934.

[8] W. Schach, Umlenkung eines kreisförmigen Flussigkeitsstrahles an einer ebenen Platte senkrecht zur Strömungsrichtung, Ing.-Arch. **6**, 51–59, 1935.

[9] Y.C. Shen, Theoretical Analysis of Jet-Ground Plane Interaction, IAS Paper No. 62-144, 1962.

[10] T. Strand, On the Theory of Normal Ground Impingement of Axisymmetric Jets in Inviscid Incompressible Flow, AIAA Paper No.64-424, 1964.

[11] M.T. Scholtz and O. Trass, Mass Transfer in a Nonuniform Impinging Jet, AIChE J. **16**, 82–96, 1970.

[12] J.H. Lienhard V, Liquid Jet Impingement, in Annual Review of Heat Transfer, C.L. Tien ed., Vol. 6, pp. 199–27, New York, Begell House, 1995.

[13] White, F. M., Viscous Fluid Flow, pp. 172–184, New York, McGraw-Hill Book Company, 1974.

[14] X. Liu, J.H. Lienhard V, and J.S. Lombara, Convective Heat Transfer by Impingement of Circular Liquid Jets, J. Heat Trans. **113**(3), 571–582, 1991.

[15] V.E. Nakoryakov, B.G. Pokusaev, E.N. Troyan, Impingement of an Axisymmetric Liquid Jet on a Barrier, Int. J. Heat Mass Tran. **21**, 1175–1184, 1978.

[16] J.H. Lienhard V and A.M. Khounsary, Liquid Jet Impingement Cooling with Diamond Substrates for Extremely High Heat Flux Applications, in High Heat Flux Engineering II, SPIE **1997**, 29–43, 1993.

[17] B.W. Blackburn, High-power target development for accelerator-based neutron capture therapy, Ph.D. Thesis in Nuclear Engineering, Massachusetts Institute of Technology, USA, 2002.

[18] J. Stevens, Y. Pan, and B.W. Webb, Effect of Nozzle Configuration on Transport in the Stagnation Zone of Axisymmetric Impinging Free-Surface Liquid Jets – Part 1: Turbulent Flow Structure, J. Heat Trans. **114**, 874–879, 1992.

[19] J. Stevens, Measurements of Local Fluid Velocities in an Axisymmetric Free Liquid Jet Impinging on a Flat Plate, Ph.D. Thesis, Brigham Young University, USA, 1991.

[20] J. Stevens and B.W. Webb, Measurements of Free Surface Flow and Structure Under an Impinging Free Liquid Jet, J. Heat Trans. **114**, 79–84, 1992.

[21] G.W. Lowery and R.I. Vachon, The Effect of Turbulence on Heat Transfer from Heated Cylinders, Intl. J. Heat Mass Trans. **18**, 1229–1242, 1975.

[22] A.B. Mehendale, J.C. Han, and S. Ou, Influence of High Mainstream Turbulence on Leading Edge Heat Transfer, J. Heat Trans. **113**, 843–850, 1991.

[23] R. Gardon and J.C. Akfirat, The Role of Turbulence in Determing the Heat Transfer Characteristics of Impinging Jets, Intl. J. Heat Mass Trans. **8**, 1261–1272, 1965.

[24] S.G. Simmons, J.M. Hager, and T.E. Diller, Simultaneous Measurements of Time-Resolved Surface Heat Flux and Freestream Turbulence at a Stagnation Point, Proc. Ninth Intl. Heat Transfer Conf., Jerusalem, Vol. 2, pp.375-380, 1990.

[25] D.T. Vader, F.P. Incropera, and R. Viskanta, Local Convective Heat Transfer From a Heated Surface to an Impinging Planar Jet of Water. Intl. J. Heat Mass Trans. **34**, 611–623, 1991.

[26] S.B. Pope, Turbulent Flows, Cambridge UK, Cambridge University Press, 2000.

[27] J. Stevens and B.W. Webb, Local Heat Transfer Coeffients Under an Axisymmetric Single-Phase Liquid Jet. J. Heat Trans. **113**, 71–78, 1991.

[28] Y. Pan, J. Stevens, and B.W. Webb, Effect of Nozzle Configuration on Transport in the Stagnation Zone of Axisymmetric Impinging Free-Surface Liquid Jets – Part 2: Local Heat Transfer, J. Heat Trans. **114**, 880–886, 1992.

[29] L.A. Gabour and J.H. Lienhard V, Wall Roughness Effects on Stagnation-Point Heat Transfer Beneath an Impinging Liquid Jet, J. Heat Trans. **116**(1), 81–87, 1994.

[30] S. Faggiani and W. Grassi, Round Liquid Jet Impingement Heat Transfer: Local Nusselt Numbers in the Region with Nonzero Pressure Gradient, Proc. Ninth Intl. Heat Transfer Conf., Jerusalem, Vol. 4, pp. 197–202, 1990.

[31] I. Silverman, Personal communication, May 2005.

[32] E.J. Watson, The radial spread of a liquid over a horizontal plane, J. Fluid Mech. **20**, 481–499, 1964.

[33] X. Liu and J.H. Lienhard V, The Hydraulic Jump in Circular Liquid Jet Impingement and in Other Thin Films, Expts. Fluids **15**, 108–116, 1993.

[34] T. Azuma and T. Hoshino, The Radial Flow of a Thin Liquid Film, Part 1: Laminar-Turbulent Transition. Bull. JSME **27**, 2739–2746, 1984.

[35] T. Azuma and T. Hoshino, The Radial Flow of a Thin Liquid Film, Part 2: Film Thickness. Bull. JSME **27**, 2747–2754, 1984.

[36] T. Azuma and T. Hoshino, The Radial Flow of Thin Liquid Film, Part 3: Velocity Profile. Bull. JSME **27**, 2755–2762, 1984.

[37] T. Azuma and T. Hoshino, The Radial Flow of Thin Liquid Film, Part 4: Stability of Liquid Film and Wall Pressure Fluctuation, Bull. JSME **27**, 2763–2770, 1984.

[38] A. Sharan, Jet-disc boiling: burnout predictions and application to solar receivers. Master's Thesis in Mechanical Engineering, University of Houston, 1984.

[39] X. S. Wang, Z. Dagan, and L.M. Jiji, Heat transfer between a circular free impinging jet and a solid surface with nonuniform wall temperature or wall heat flux-2. solution for the boundary layer region, Int. J. Heat Mass Trans. **32**(7), 1361–1371 1989.

[40] X. Liu and J.H. Lienhard V, Liquid Jet Impingement Heat Transfer on a Uniform Flux Surface, Heat Transfer Phenomena in Radiation, Combustion, and Fires, ASME-HTD Vol. 106, pp. 523–530, 1989.

[41] Z.H. Chaudhury, Heat transfer in a radial liquid jet, J. Fluid Mech. **20**, 501–511, 1964.

[42] M. Errico, A study of the interaction of liquid jets with solid surfaces, Ph.D. thesis, University of California, San Diego, USA, 1986.

[43] J.H. Lienhard V, X. Liu, and L.A. Gabour, Splattering and Heat Transfer During Impingement of a Turbulent Liquid Jet, J. Heat Trans. **114**(2), 362–372, 1992.

[44] D.A. Varela and J.H. Lienhard V, Development of non-linear waves on a non-uniform axisymmetric film. Bulletin of American Physical Society, AI8, **36**(10), November 1991.

[45] S.K. Bhunia and J.H. Lienhard V, Splattering during Turbulent Liquid Jet Impingement on Solid Targets, J. Fluids Engnrg. **116**(2), 338–344, 1994.

[46] S.K. Bhunia and J.H. Lienhard V, Surface Disturbance Evolution and the Splattering of Turbulent Liquid Jets, J. Fluids Engnrg. **116**(4), 721–727, 1994.

[47] G.K. Batchelor, The Theory of Homogeneous Turbulence, Cambridge UK, Cambridge University Press, 1953.

[48] A.M. Yaglom, An Introduction to the Theory of Stationary Random Functions, New York, Dover, 1973.

[49] George, W.K., Beuther, P.D,, and Arndt, R.E.A., Pressure spectra in turbulent free shear flows, J. Fluid Mech. **148**, 155–191, 1984.

[50] X. Liu and J.H. Lienhard V, Extremely High Heat Fluxes Beneath Impinging Liquid Jets. J. Heat Trans. **115**(2), 1993, pp.472–476.

[51] C.H. Oh, J.H. Lienhard V, H.F. Younis, R.S. Dahbura, and D. Michels, Jet-Array Cooling Modules for High Flux Removal. AIChE J. **44**(4), 1998, pp. 769–779.

[52] J.H. Lienhard V and J. Hadeler, High Heat Flux Cooling by Liquid Jet Array Modules. Chem. Engnrg. & Tech., **22**(11), 967–970, 1999.

[53] J.H. Lienhard V and D.S. Napolitano, Yield Limits of Plates at Extremely High Heat Fluxes. J. Heat Trans. **120**(1), 253–258, 1998.

[54] D. Michels, J. Hadeler, and J.H. Lienhard V, High Heat Flux Resistance Heaters produced by VPS and HVOF Thermal Spraying. Exptl. Heat Trans. **11**, 341–359, 1998.